The Role of Fluid Pressure-Induced Aseismic Slip in Earthquake Cycle Modulation

S. K. Y. Lui[1,2] , **Y. Huang[3]** , **and R. P. Young[2,4,5]**

[1]Department of Chemical and Physical Sciences, University of Toronto, Mississauga, ON, CA, [2]Department of Earth Sciences, University of Toronto, Mississauga, ON, CA, [3]Department of Earth and Environment Sciences, University of Michigan, Ann Arbor, MI, CA, [4]Department of Civil and Mineral Engineering, University of Toronto, Mississauga, ON, CA, [5]Department of Physics, University of Toronto, Mississauga, ON, CA

Abstract The evolving state of fault stress during and after the perturbation of fluid pressure gives rise to an intriguing interplay of seismic and aseismic slip on the fault. A better understanding of the possible role of fluids in the triggering mechanism of seismicity is pivotal to effective seismic hazard mitigation, particularly in the context of induced seismicity. Through numerical modeling, we investigate the effect of pore pressure perturbations on the spatio-temporal evolution of fault slip and the modulation of earthquake cycles. Pressure perturbations are imposed at different magnitudes and different times during a selected interseismic period. Results show a wide range of aseismic responses which can lead to both time advancement and delay of subsequent earthquakes. Specifically, even pressure perturbation <5% of the average event stress drop can trigger aseismic slip that leads to considerable time delay in the next earthquake even when perturbation occurs late in the interseismic period. We find that earthquakes that are delayed in time are associated with large aseismic moment release. Our study highlights the importance of close monitoring of aseismic fault slip in regions prone to the influence of pore fluids and provides physical insights into identifying critical aseismic responses associated with certain triggering outcomes.

1. Introduction

For many years, aseismic slip has been found to play a significant role in fault slip evolution and contribute to interesting phenomena in different geological settings (Byrne et al., 1992; Chen & Lapusta, 2009; Igarashi et al., 2003; Jolivet et al., 2015; Lui & Lapusta, 2018; Nadeau & Johnson, 1998; Rousset et al., 2016; Schmidt et al., 2005). At subduction zones, the extent of downdip region exhibiting aseismic behavior has important implications for the seismic hazard on the megathrust faults (Byrne et al., 1992). In regions previously thought to be under steady loading, bursts of aseismic transient discovered from InSAR or geodetic data highlight the needs to revise our understanding on the underlying fault mechanics (Rousset et al., 2016). Many repeating earthquake sequences are found to exhibit atypical scaling between recurrence time and seismic moment due to significant aseismic slip in the seismogenic regions (Chen & Lapusta, 2009; Lui & Lapusta, 2018; Nadeau & Johnson, 1998). In tectonic earthquakes, aseismic slip is often found be operating in combination with pore pressure diffusion as driving processes (De Barros et al., 2020; Duverger et al., 2018; Hatch et al., 2020; Ruhl et al., 2016).

In the context of injection-induced seismicity, recent studies also suggest complex triggering mechanisms involving aseismic motion induced on or surrounding the fault (Cappa et al., 2019; De Barros et al., 2016; Duboeuf et al., 2017; Eyre et al., 2019; Goodfellow et al., 2015; Guglielmi et al., 2015; Huang et al., 2019; Wei et al., 2015). For example, joint analysis of seismic data, radar and leveling measurements shows that the M_w 5.3 and 5.4 main shocks of the Brawley swarm in 2012 are preceded by aseismic slip on a neighboring fault that is closer to the injection well (Wei et al., 2015). Field experiment which involves measuring fault slip and seismicity induced by fluid injection into a natural fault reveals that microseismic activities are preceded by a considerable amount of aseismic slip (Guglielmi et al., 2015), and further analysis on the observations infers that the large aseismic slip in this injection experiment may promote localized stress transfer and induced microearthquakes with low relative stress drops (Huang et al., 2019). Numerical modeling finds that fluid-induced aseismic slip front can outpace pore-fluid migration and transmit earthquake-triggering stress changes beyond the fluid-pressurized zone (Bhattacharya & Viesca, 2019). At the laboratory

scale, studies have shown that fluid injection experiments on granite samples under triaxial stresses result in substantial aseismic deformation during fluid pressurization (Goodfellow et al., 2015). Nonetheless, with the complexity of the earth's crust it remains challenging to dissect the interaction between aseismic and seismic motions and in particular, how pore pressure perturbation may affect aseismic slip and earthquake cycles remains elusive.

The classic notion on the effect of pore pressure perturbation is earthquake cycle advancement. As fluid migrates through high-permeability pathways to local fractures zones, the direct effect of an increase in pore pressure (p) reduces the effective normal stress of the fault and hence the fault resistance (Parotidis et al., 2003; Shapiro et al., 2002). Other mechanisms such as the propagation of fracture through hydrofracturing (Cornet, 2000) and poroelastic stress perturbation due to fluid extraction or injection, which does not require direct hydrological connection (Goebel et al., 2017; Segall, 1989), bring the fault closer to failure and leads to a time advancement of the next earthquake by either lowering the fault strength or increasing the loading of stress. When accounting for triggered aseismic slip, however, it can be a more complex scenario. Aseismic motions do not always directly trigger seismic slip, but may weaken the fault without noticeable signals and affect the occurrence of future earthquakes. If the stress released due to aseismic motion is substantial, can it potentially delay subsequent seismic cycle(s)? Moreover, how would a fault respond seismic- and aseismically to stress perturbations occurring at different magnitudes and at various stages of the interseismic period?

In this study, we investigate the effect of pore pressure perturbation on the interaction of aseismic and seismic motions on the fault, and how such interactions can change the temporal evolution of earthquake cycles and the nucleation of dynamic ruptures on the fault. We simulate sequences of earthquakes using fully dynamic earthquake cycle simulations, which resolve the spontaneous slip history of a rate-and-state planar fault under stable tectonic loading. Our model features a fault subjected to external stress perturbation and generating $M_w \sim 3$ earthquake sequences. $M_w \sim 3$ earthquakes are commonly observed earthquake sizes in the central US before the surge of induced seismicity. The temporal rate of change of seismicity has clear association with fluid injection in the region, and their migration during an induced seismicity sequence is insightful for the delineation of fault strands. We examine stress perturbation occurring throughout a seismic cycle, with specific focus on combinations of variables that may match realistic field conditions. For example, it is commonly believed that faults in the central US are critically stressed and that tectonic-like events can be induced by negligible changes in the state of stress due to the presence of fluid (Townend & Zoback, 2000). Also, the inferred change in p due to fluid injection is within 0.01–1 MPa (Hearn et al., 2018; Keranen et al., 2014), which is a very small percentage of typical stress drops of induced events ranging between 1 and 20 MPa (Boyd et al., 2017; Huang et al., 2017; Wu et al., 2018). Therefore, modeling fault response to small stress perturbation at later stages of the cycle can provide physical insights into the mechanisms of induced seismicity.

2. Models and Methods

2.1. Fault Governed by the Rate-and-State Friction

Our numerical model adopts the empirically derived rate-and-state friction laws (Dieterich, 1979; Marone, 1998; Ruina, 1983), which are capable of modeling and explaining both seismic and aseismic phenomena (Ben-Zion & Rice, 1997; Dieterich, 1994; Gomberg et al., 1998; Lapusta et al., 2000; Lapusta & Liu, 2009; Lapusta & Rice, 2003; Miyazaki et al., 2006; Rice & Ruina, 1983). In the formulation, the shear stress (τ_f) on the fault is given by

$$\tau_f = \overline{\sigma} f = \left(\sigma - p \right) \left[f_o + a \, ln \left(\frac{V}{V_o} \right) + b \, ln \left(\frac{V_o \theta}{L} \right) \right] \tag{1}$$

where $\overline{\sigma}$ is the effective normal stress, σ is the normal stress, p is the pore pressure, f is the friction coefficient, f_o is the reference friction coefficient at the reference slip velocity V_o, and a and b are rate-and-state parameters, V is slip velocity, and L is the characteristic slip for the evolution of the state variable θ. The evolution of the state variable θ in our model is governed by the aging formulation:

$$\frac{d\theta}{dt} = 1 - \frac{V\theta}{L} \tag{2}$$

In steady state, that is, when V is constant, one gets $\theta = L / V$ and the resulting shear resistance τ_{ss} is

$$\tau_{ss} = \bar{\sigma}\left[f_o + \left(a - b\right)ln\left(\frac{V}{V_o}\right)\right] \tag{3}$$

Thus, the fault behavior at steady state is defined by the value of parameter $\left(a - b\right)$. $a - b > 0$ corresponds to velocity-strengthening (VS) frictional properties, resulting in stable slip at the imposed loading rate, while $a - b < 0$ corresponds to velocity-weakening (VW) friction, and for VW area of sufficiently large sizes, results in potentially seismogenic regions (Rice et al., 2001; Rice & Ruina, 1983; Rubin & Ampuero, 2005). In the framework of rate-and-state friction, shear stress is assumed to be equal to frictional strength on the fault.

Dynamic instability develops when the steady-state VW slipping region of the fault is larger than the nucleation size. Here we utilize the theoretical estimate of nucleation size established by Rubin and Ampuero (2005), with the additional factor of $\pi^2 / 4$ to account for 3-dimensional simulations (h_T^*):

$$h_T^* = \frac{\pi^2}{4} \frac{2\mu^* bL}{\pi\bar{\sigma}\left(b - a\right)^2} \tag{4}$$

where $\mu^* = \mu$ for mode III ruptures and $\mu^* = \mu / \left(1 - \upsilon\right)$ for mode II ruptures, μ is the shear modulus, and υ is the Poisson's ratio. This 3-D estimate has been shown to match the combined nucleation sizes produced by 3-D earthquake simulations (Chen & Lapusta, 2009).

In our model, a strike-slip planar fault is embedded in a 3-D elastic medium (Figure 1a). Using spectral boundary-integral methodology with adaptive time stepping (Lapusta et al., 2000; Lapusta & Liu, 2009), we solve for the spontaneous shear stress and slip history on the fault, resolving all aspects of seismic and aseismic slip at different stages of the seismic cycle, all inertial effects during simulated earthquakes with slip rate of the order of meters per second, and postseismic slip. Our fully elastic model ignores the viscous response of the crust and assumes postseismic relaxation in the form of afterslip. It has been successfully applied to reproduce various earthquake phenomena in both field and laboratory scales (Barbot et al., 2012; Lui & Lapusta, 2016, 2018; Noda & Lapusta, 2013; Schaal & Lapusta, 2019).

2.2. Spatio-Temporal Resolution of Numerical Model

To capture the evolution of shear stress and slip rates in the fully dynamic model, both the cohesive zone (Λ_0) and the nucleation size (h_T^*), have to be properly resolved, which are important in dynamic rupture (Day et al., 2005; Lapusta & Liu, 2009) and during interseismic periods (Ben-Zion & Rice, 1997; Lapusta et al., 2000; Rice & Ruina, 1983), respectively. Day et al. (2005) established that the initial cohesive zone size has to be discretized by at least three to five spatial cells (Δx). The cell size in our model is approximately one-fifth of the estimated cohesive zone size, which allows us to accurately simulate seismic events in our models. According to Equation 4, h_T^* of our model is ~190 times of Δx, which also exceeds the criterion for obtaining resolution-independent results. We further compare our model against one with cell size = 0.5 Δx, which yields almost identical results, and hence confirm the robustness of our model in terms of spatial resolution.

For proper temporal resolution under variable time stepping, we employed the procedure developed by Lapusta et al. (2000) and utilize a minimum time step estimate of $\Delta t_{\min} = \gamma\Delta x / C_s$, where $\gamma = 1 / 3$, which is capable of producing good resolution of dynamic rupture propagation as suggested by Day et al. (2005). The 3-D boundary integral modeling employs the BICycle algorithm developed by Lapusta and Liu (2009) and is performed in parallel on 128 cores, each with a memory of 5 GB. For the fault model in this study, a simulated period of ~20 years takes 10 computational hours to run.
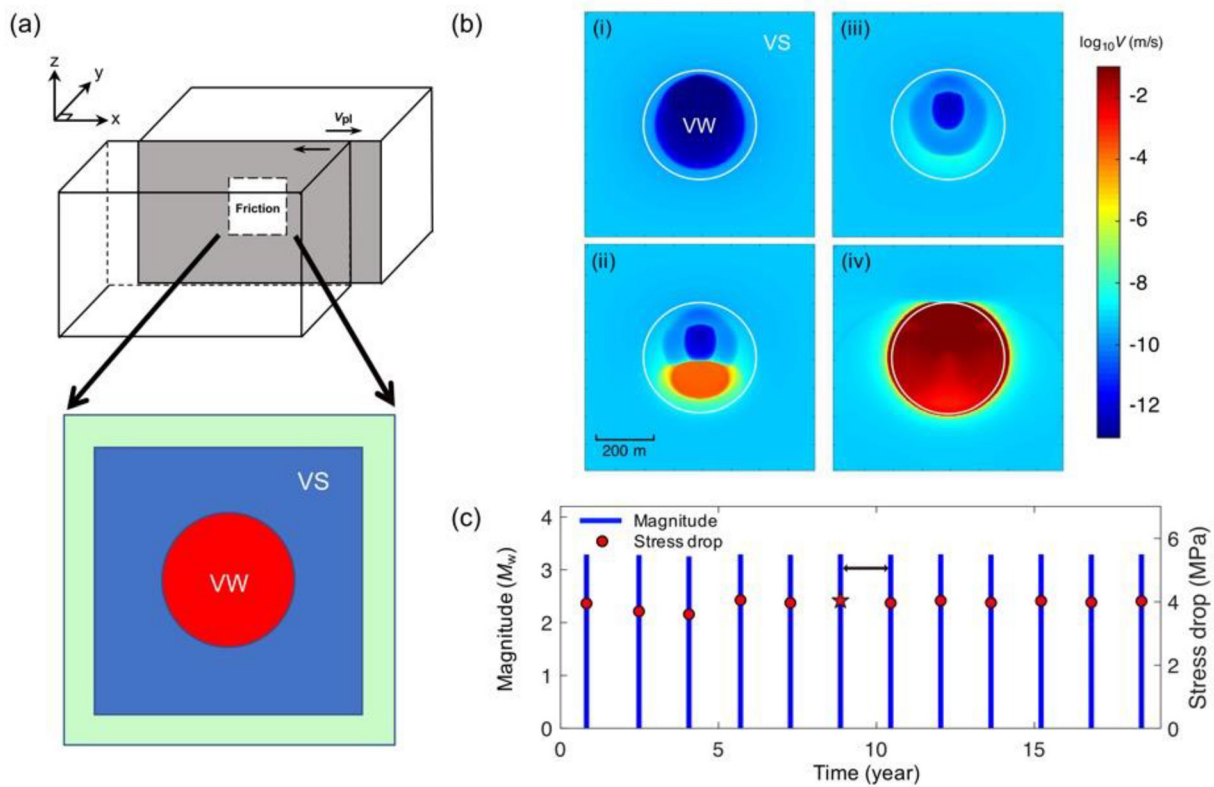
Figure 1. Schematics of the fault model and the unperturbed earthquake sequence in our simulations. (a) (Top) In the numerical model, a planar strike-slip fault (region where friction acts) is embedded into a 3-D homogeneous elastic medium (bottom). In our study, a (red) circular VW patch is centered inside the (blue) creeping VS region. Stable plate-rate loading is transmitted from the (green) boundary region. (b) Snapshots (i–iv) illustrate a typical seismic event of the earthquake sequence that ruptures the entire velocity-weakening patch. This is the sixth event of the sequence (red star in Figure 1c). Color scale indicates slip rate on the fault. (c) Moment magnitude and stress drop of the tectonic earthquake sequence generated on the numerical fault with no external stress perturbation. VS, velocity-strengthening; VW, velocity-weakening.

2.3. Fault Model Setup

In the model, the fault is divided into three regions: The location of the induced earthquake sequence is represented as a circular VW patch, embedded in the center of a VS creeping region, by assigning VW properties, $a - b < 0$, to the VW patch and VS properties, $a - b > 0$, to the surrounding fault zone. There is also a boundary region where a fixed tectonic loading rate is applied (Figure 1a). The VW patch has a diameter of 400 m, and the adjacent VS region is driven by steady sliding at a rate of 23 mm per year. The effective normal stress on the fault is 50 MPa, approximating the stress condition at a crustal depth of 3 km, which is within the common range of focal depth for induced earthquakes in the central US. The full list of model parameters, including fault properties and frictional parameters commonly used in simulations, are listed in Table 1.

In the simulation, slip at each time step that occurs with slip rate of 0.01 m/s or higher is considered seismic, which is consistent with previous studies (Bizzarri & Belardinelli, 2008; Lapusta & Liu, 2009; Noda & Lapusta, 2013; Rubin & Ampuero, 2005). The rest of slip is considered aseismic. Hence, each seismic event begins in the simulation when slip rate of 0.01 m/s is reached at one or more points on the fault, and ends when slip rate everywhere on the fault first decreases to less than 0.01 m/s. Stress drop is defined as the difference between shear stresses at the beginning and end of a seismic event. The average stress drop for each seismic event is computed as a moment-based average (Noda et al., 2013).

Table 1
Fault Model Parameters Used in all Simulations

Parameter	Symbol	Value
Shear wave speed	C_s	3.0 km/s
Shear modulus	μ	30 GPa
Reference slip velocity	V_o	10^{-6} m/s
Reference friction coefficient	f_o	0.6
Characteristic slip distance	L	160 μm
Rate-and-state parameters in VW region	a_{vw}, b_{vw}	0.015, 0.019
Rate-and-state parameters in VS region	a_{vs}, b_{vs}	0.019, 0.015
Cell size	Δx	0.96 m

2.4. Tested Model Space

In cases without external stress perturbation, seismic events rupture the entire seismogenic velocity-weakening (VW) region of 400 m in diameter (Figure 1b). In the simulations, all initial loading conditions are relaxed over the first three cycles, allowing the model to stabilize to a repeating sequence with consistent recurrence interval and source properties after ∼5 years. The generated tectonic sequence has an average moment magnitude and stress drop of M_w 3.3 and 4 MPa, respectively (Figure 1c). These source properties are comparable to the commonly reported earthquakes in the central and eastern United States (Huang et al., 2017). The average recurrence interval of the sequence of events is 1.61 years, which is defined as the time window between the onset of a dynamic event, that is, seismic wave energy being emitted, and the end of the interseismic period that follows, that is, right before the next earthquake occurs.

Based on the unperturbed tectonic sequence, we impose pore pressure perturbation during the sixth earthquake cycle, that is, the interseismic period between the sixth and seventh earthquakes of the sequence (black arrow in Figure 1c), well into the stage in which a stable repeating sequence is established. Our main focus is the fault response to perturbations with different magnitudes that occur at various times during an earthquake cycle. Therefore, we only vary two parameters in the model: the magnitude of the perturbation and the timing of perturbation relative to an unperturbed seismic cycle. For mathematical simplicity, a single pore pressure change is imposed as an instantaneous positive step increase uniformly across the entire fault (Δp) during the selected earthquake cycle. More complex perturbation patterns that account for parameters such as the rate of pressure change and the frequency of perturbation are not included.

The magnitude of pore pressure perturbation depends on factors such as injection rate, distance from injection sites and hydraulic diffusivity of the crust. Using hydrogeological models, Keranen et al. (2014) inferred a range of pore pressure perturbation between 0.01 and 1 MPa for the Jones swarm near West Carney field, Oklahoma. Keranen and Weingarten (2018) also showed several possible scenarios of pore fluid pressure variation and the magnitude can be over 1 MPa at distances within 1 km from the well. Here we adopt a range of positive change in pore pressure (Δp) between 0.01 and 2 MPa, which is equivalent to 2.5%–50% of the average stress drop of the simulated sequence. In terms of perturbation time, T_p is defined as the time of perturbation with respect to an unperturbed seismic cycle: A perturbation imposed at X% of a selected seismic cycle is abbreviated as $T_p = $ X%. T_p in our simulations is between 25% and 90% of the interseismic period. We analyze the behavior of the source region and changes in the source characteristics and temporal distribution of the perturbed sequence. The percentage change in the perturbed cycle durations relative to the averaged unperturbed seismic cycle (ΔT_r) is defined as

$$\Delta T_r = \frac{T_{nr} - T_{ur}}{T_{ur}} \times 100\% \tag{5}$$

where T_{ur} is the unperturbed recurrence interval, and T_{nr} is the new recurrence interval under the influence of perturbed stresses. A negative ΔT_r indicates a time advancement of the next earthquake, and vice versa.

3. Results

3.1. Effects of Pore Pressure Perturbation on the Timing of Triggered Earthquakes

For a $\Delta p = 2$ MPa, that is, 50% of the average stress drop, time advancement to the next earthquake is significant regardless of T_p, resulting almost always in instantaneous triggering (Figure 2a). Instantaneous triggering refers to the nucleation of the next earthquake starting right after perturbation is applied and the eventual dynamic rupture occurring within hours. For perturbation magnitude between 10%–25% of the average event stress drop, that is, $\Delta p = 0.5$ and 1 MPa, we generally observe a time advancement to the next earthquake, except for one case with $\Delta p = 1$ MPa. For cases with 25% < T_p < 60%, there is as much as a 40% time advancement (ΔT_r is up to −40%). Within the last quarter of the cycle, that is, 75% < T_p < 90%, the fault is already critically stressed, and hence seismic events are triggered instantaneously. As a feature under the rate-and-state friction, the time remaining to instability after the stress perturbation is nonlinear and exceeds the estimation based on the assumption of a linear relationship between the interevent time
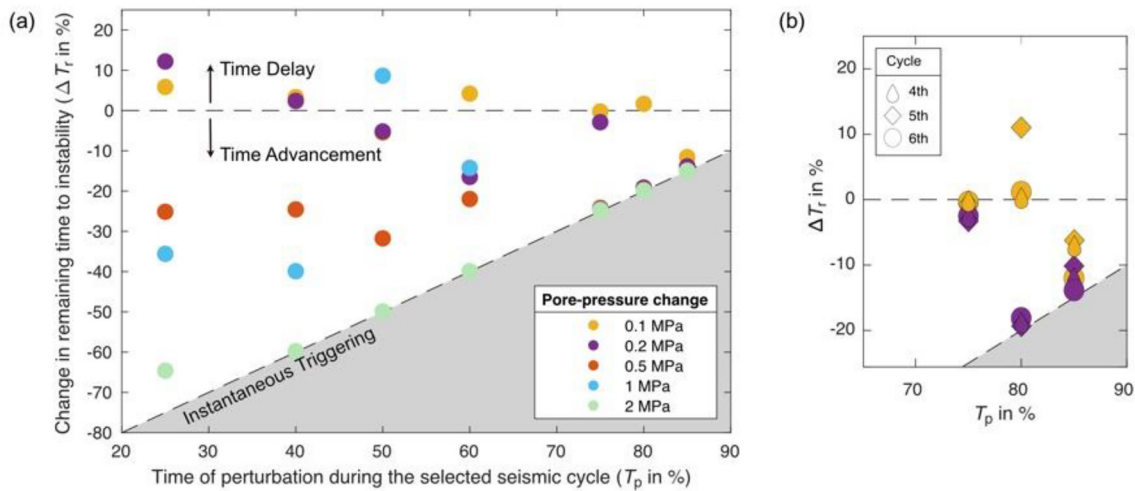
Figure 2. Change in the remaining time to instability with respect to pore pressure perturbed at different times during the selected seismic cycle. (a) Each data point represents one simulation within the tested model space. Markers falling on or very close to the dashed edge of the gray triangle are events that are instantaneously triggered. (b) Simulation results with pore pressure perturbation at 0.1 MPa (yellow markers) and 0.2 MPa (purple markers) implemented at fourth, fifth and sixth cycles.

and the inverse of stress loading rate. This indicates that additional factors are likely to contribute to the occurrence time of the triggered event, such as fault aseismic motion.

For $\Delta p \leq 0.2$ MPa, that is, < 5% of the average event stress drop, we see more contrasting responses wherein ΔT_r can be negative or positive at different T_p. For $\Delta p = 0.2$ MPa, time delay occurs when $T_p \leq 40\%$. On the other hand, in the majority of scenarios with $\Delta p = 0.1$ MPa, there is a time delay. In particular, even when perturbations occur late in the interseismic period, instead of bringing the fault to failure, we find that the remaining time to the next event is lengthened in some cases. To this end, we also explore more scenarios by perturbing the same time window in the fourth and fifth seismic cycles of the unperturbed sequence, and find that T_{nr} can be over 10% longer than T_{ur} when $T_p = 80\%$ (Figure 2b). At this stage of the cycle, a small difference in T_p can reverse the scenario from delay to advancement. For example, for $\Delta p = 0.1$ MPa that occurs during the fifth cycle, T_r is positive (>10%) when $T_p = 80\%$, but is negative (−5%) when $T_p = 85\%$ (Figure 2b). In Section 3.3, we discuss how the modulation of seismic cycle, particularly the delaying of subsequent earthquakes, is due to triggered aseismic slip in the VW region.

3.2. Effects of Pore Pressure Perturbation on Earthquake Source Properties and Nucleation Process

Our simulation results indicate that the changes in pore pressure, even up to 50% of the average event stress drop, have no significant effect on the magnitude or the stress drop of the triggered earthquakes. The magnitude ranges from Mw 3.18 to 3.41, and the stress drop ranges from 2.8 to 4.2 MPa (Figure 3). This is likely because the event magnitude is constrained by the size of the VW patch preset in the model setup, as well as the frictional properties of the VS region, which controls how far the coseismic slip can penetrate into the surrounding VS region. For example, for larger $(a) - (b)_{VS}$, we would expect stronger suppression of the propagating slip front and hence a smaller extent of penetration into the VS region. This would imply a smaller total rupture area, and hence a higher average stress drop.

On the other hand, among the triggered events with a narrow range of magnitude, we observe considerable difference in the nucleation process. According to Equation 4, the theoretical estimate of nucleation size (h_T*) in the current model set up is ~180 m, so the ratio between the VW patch and h_T* of the fault in our model is ~2.2. We investigate how nucleation size changes under the influence of pore pressure change. To measure the actual nucleation size resolved in the simulations ($h*$), we determine the edge of the nucleating region to be where $\log_{10}(V)$ drops off rapidly (black dotted outline in Figure 4a). Based on the outlined area,
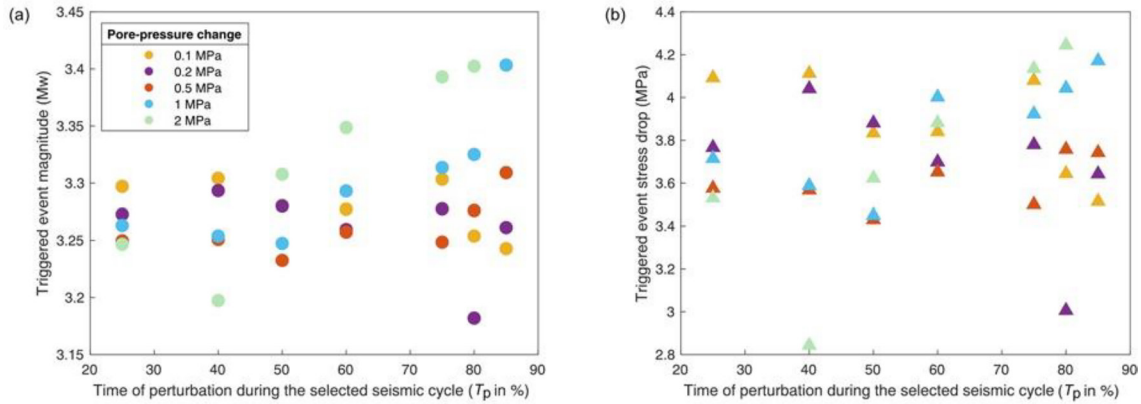
Figure 3. Source properties of triggered earthquakes. (a) Earthquake magnitude of triggered earthquakes. (b) Earthquake stress drop of triggered earthquakes.

an effective diameter is back-calculated using Equation 4, assuming the area to be a circle. In the case with no perturbation, h^* is ~183 m, very similar to h_T^*. Among all simulated cases, h^* of the triggered earthquakes ranges between 40% and 160% of h^* of the unperturbed event (Figure 4b). This shows that the nucleation evolution and size are strongly controlled by the loading history of the fault. While h^* is similar to h_T^* under slow tectonic loading, relatively small perturbations can make substantial differences. There is no obvious correlation between h^* and T_p, but h^* is negatively related to triggered event magnitude (Figure 5). This is likely because for cases with large h^*, substantial slip has occurred within the VW region before the onset of the dynamic rupture (Figure S1a), which partially releases the cumulative stress and results in a smaller seismic event. In contrast, a smaller h^* implies much less slip preceding the dynamic rupture, resulting in more stress being released during the seismic event and a larger mainshock (Figure S1b). The observed difference in slip rate evolution and nucleation process is the outcome of the triggered aseismic response due to pore pressure perturbation, which is discussed in the next section.

3.3. Critical Role of Fluid-Induced Aseismic Slip

Next we investigate how aseismic slip on the fault may drive the observed variations in the perturbed seismic cycle. Specifically, we analyze the temporal evolution of aseismic moment released on the VW region by
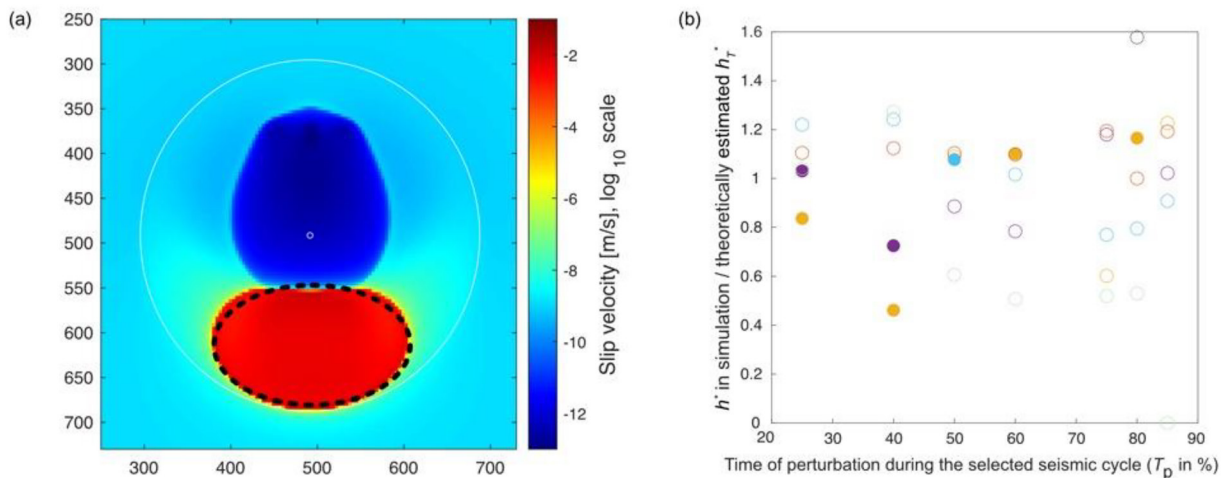

Figure 4. Change in nucleation size (h^*) of triggered earthquakes. (a) Simulation with $\Delta p = 0.5$ MPa and $T_p = 80\%$. Snapshot showing the slip velocity in the VW region (white circle) at the onset of a dynamic rupture, that is, as soon as one or more cells are slipping above the threshold seismic rate (0.01 m/s). The nucleation region is outlined by the black dotted line, where $\log_{10}(V)$ drops off rapidly. Unit of x- and y-axis is meter. (b) h^* in simulations, with respect to theoretically estimated h_T^*, versus T_p. Filled and empty markers represent cases with a time delay and advancement, respectively.
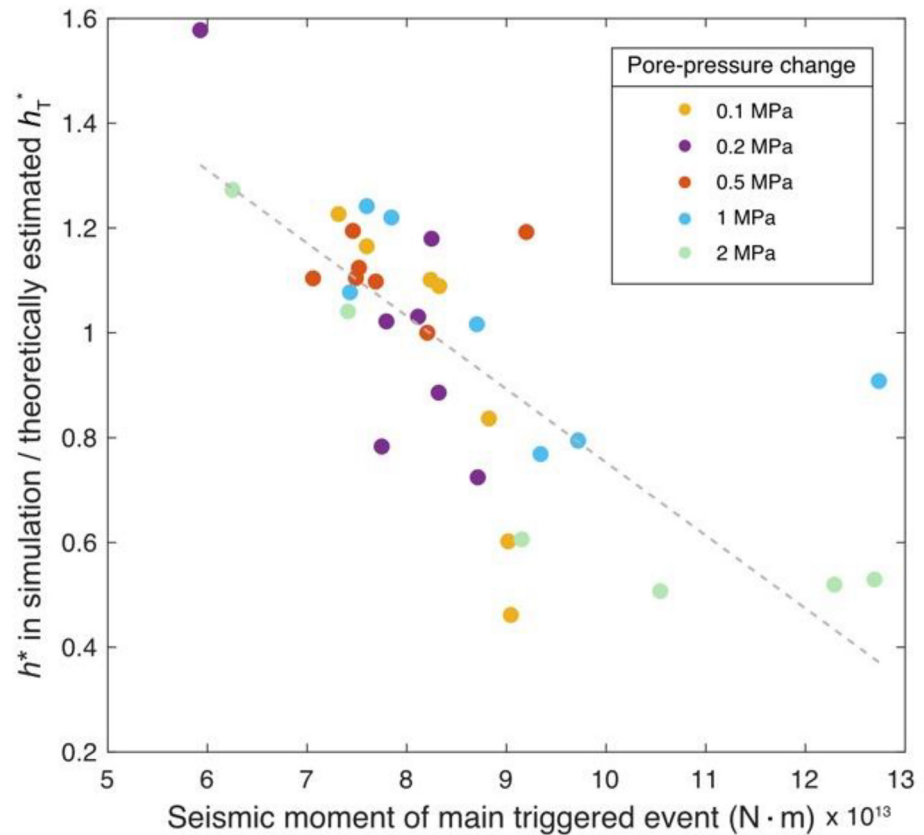
Figure 5. Nucleation size versus magnitude of triggered events. $h*$ in simulations, with respect to theoretically estimated h_T*, versus seismic moment of triggered events. Gray dashed line is the best-fitting line, with linear equation $y = -0.1394\,x + 2.1465$ and coefficient of determination $R^2 = 0.6$.

cells slipping below the threshold seismic velocity (0.01 m/s) during each time step. Our key finding is that, independent of the magnitude and timing of perturbation, there is a general positive correlation between the aseismic moment released during the perturbed cycle and the change in T_r, that is, delayed triggered events are preceded by higher aseismic moment release (Figure 6). In the two scenarios in which the triggered events experience the longest time delay (by ~10%), the slow slip events release aseismic moment exceeding 8×10^{13} N·m, which is comparable to the average event size of the sequence (M_w 3.3).

Under the rate-and-state friction, the extent of aseismic response and the time remaining to instability strongly depends on the stress state of the asperity at the onset of stress perturbations. Particularly, for perturbations occurring late in the interseismic period, we see significant variations in the triggered aseismic slip with only 5% difference in T_p, which results in contrasting outcomes, that is, event advancement versus delay. This can be illustrated with two scenarios during the fifth seismic cycle, with $\Delta p = 0.1$ MPa and $T_p = 80\%$ and 85%, respectively. When $T_p = 80\%$, the fault experiences two major aseismic transients after the perturbation, which significantly prolong the time remaining to instability (Figure 7a). At the time of perturbation, aseismic creep in the surrounding VS area due to far-field loading has started penetrating radially into the VW region. At the same time, there is also a weak aseismic creep front propagating upward around the locked region at the center (Figure 7b, snapshot 1). Pore pressure perturbation happening coincidentally with the development of an aseismic transient has led to a strong one, with maximum slip rate reaching 10^{-5} m/s (Figure 7b, snapshot 2). Nonetheless, since slip rate of the centered locked area remains at ~10^{-13} m/s and the area is a significant portion (25%) of the VW region, the condition is not favorable for the aseismic transient to nucleate into a dynamic rupture. Afterward, the VW patch stabilizes and returns to a locked condition (Figure 7b, snapshot 3). With this stress condition, the second aseismic transient also fails to develop into a seismic event (Figure 7b, snapshot 4). Note that this transient is also weaker than the
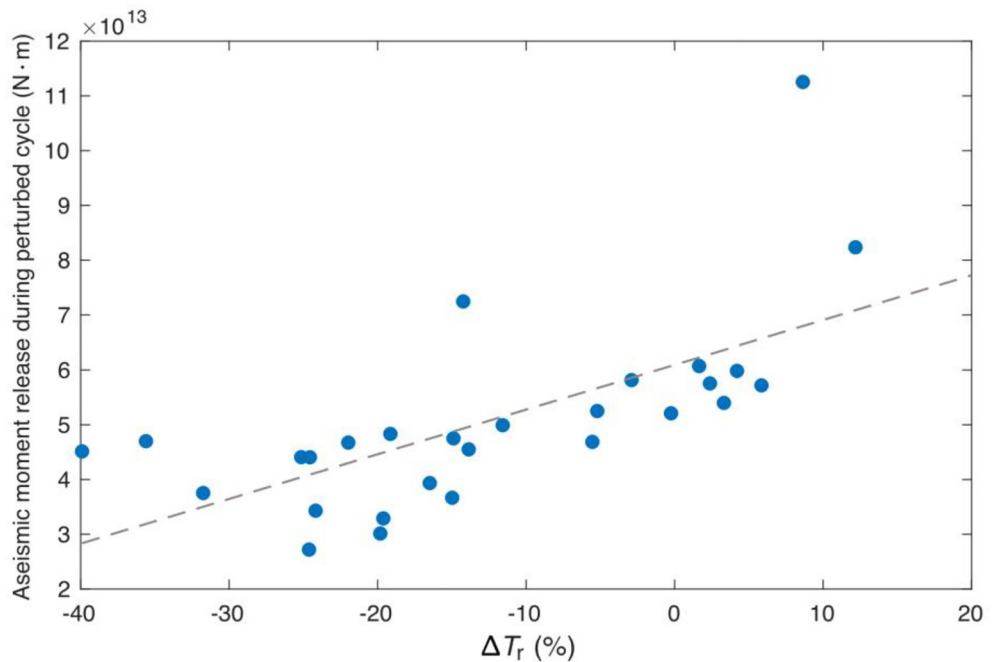
Figure 6. Aseismic moment released in the VW region during the perturbed cycle. There is a positive correlation between the aseismic moment released and ΔT_r. The gray dashed line is the best fitted line.

first one with a lower maximum slip rate. The VW region then stabilizes again, but slip rate of the locked region further increases (Figure 7b, snapshot 5). A seismic nucleation eventually starts on day 184 post perturbation, but the interplay of aseismic transients and fault stabilization is substantial enough to delay the triggered event timing by 10% (Figure 7b, snapshot 5–6).

Perturbation at $T_p = 85\%$, on the other hand, coincides with the end of a weak aseismic transient, and hence there is no direct triggering of significant aseismic moment release (Figure 8a). However, at the onset of perturbation, only 16% of the VW region remains locked (area in dark blue). Creep has penetrated substantially into the remaining area and causing it to slip at close to the fixed tectonic loading rate (Figure 8b, snapshot 1). Together with the slight increase in overall slip rate due to pore pressure perturbation, the fault is under a condition which prevents it from stabilizing (Figure 8b, snapshot 2). Therefore, as slip starts accelerating at the bottom of the VW patch, an advanced dynamic rupture develops on day 52 post perturbation (Figure 8b, snapshot 3).

To quantify the role of aseismic slip, we examine the frequency and intensity of aseismic transients that occur between T_p and the next triggered event. First of all, the unperturbed tectonic sequence has a relatively simple aseismic moment release pattern in every seismic cycle, as indicated by the rate of moment release and the change in maximum slip rate on the fault (Figure S2). There is only one obvious occasion when the rate of aseismic moment release picks up slightly at ~85% of the cycle, during which the maximum slip rate on the fault increases by less than two orders from $\sim10^{-9}$ to $\sim10^{-7.5}$ m/s. When pore pressure is perturbed, even at small magnitudes of 0.1 and 0.2 MPa, it is obvious that significantly more complex moment release patterns can be induced. For example, when $T_p = 25\%$, there are up to four aseismic transients between T_p and the next triggered event (Figures S3). We find that the timing of subsequent triggered earthquakes is not dependent on the frequency but the intensity of aseismic transients, as expressed by the change in maximum slip rate within the VW region. In particular, for smaller perturbation magnitudes in our model space, that is, $\Delta p = 0.1$ and 0.2 MPa, aseismic transients associated with delayed induced earthquakes in general have higher maximum slip velocity than those associated with earthquake time advancement. For $T_p < 75\%$, earthquakes tend to be advanced if the triggered aseismic transients do not exceed a critical slip rate of 10^{-6} m/s (Figures 9a, S4). For $T_p \geq 75\%$, the maximum transient slip rate associated with advanced earthquakes also slightly increases, but in general they are still lower than those associated with delayed
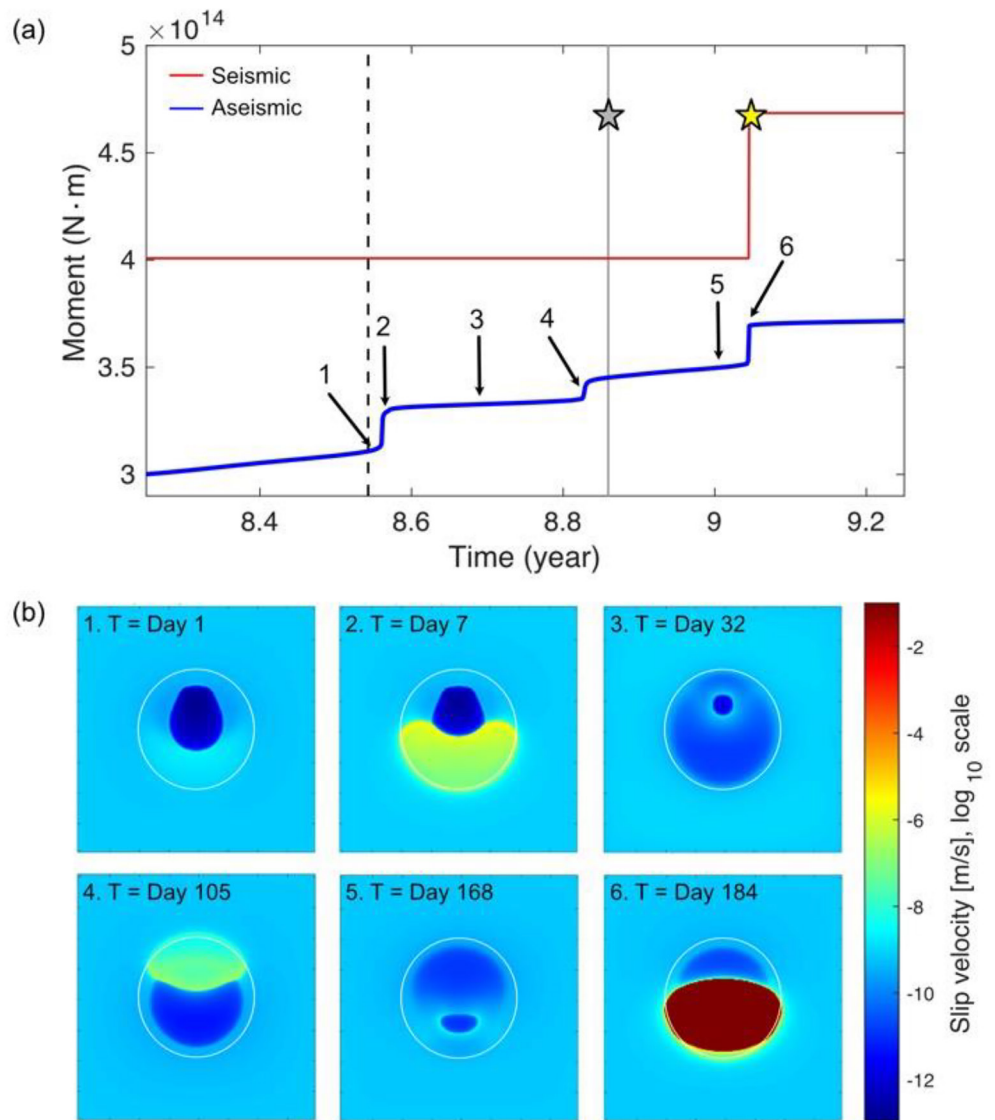
Figure 7. Simulation with $\Delta p = 0.1$ MPa and $T_p = 80\%$ (imposed in the fifth cycle) that results in a delay of the triggered event. (a) The release of seismic and aseismic moment during the perturbed cycle. In this case, pore pressure is 0.1 MPa and $T_p = 80\%$. Yellow star represents the occurrence of the triggered event, which marks the beginning of the next cycle. The gray star and gray line represent the timing of the sixth event in the unperturbed sequence. In this case, the triggered event experiences a time delay. Black dashed line marks T_p. Slip rate on the fault at six specific times, as pointed out by the black arrows, is shown in snapshots in (b). (b) Snapshots illustrating the slip evolution on the VW patch after pore pressure is perturbed. VW, velocity-weakening.

cases (Figure 9a). For larger perturbation magnitudes, that is, 0.5 and 1 MPa, the intensity of aseismic transients associated with earthquake advancement becomes even stronger, up to the order of 10^{-3} m/s (Figures 9b, S5). Due to the larger magnitude of pressure change, all the earthquakes are instantaneously triggered for $T_p \geq 75\%$.

Another interesting observation is that for cases with the most delayed earthquakes, that is, $\Delta T_r \approx 10\%$, the intensity of aseismic transients is very strong, with maximum slip velocity momentarily reaching the dynamic slip rate threshold preset in the model. For instance, in the rare case of $\Delta p = 1$ MPa at $T_p = 50\%$, in which the triggered event is delayed by almost 10%, the induced aseismic transients are so strong that
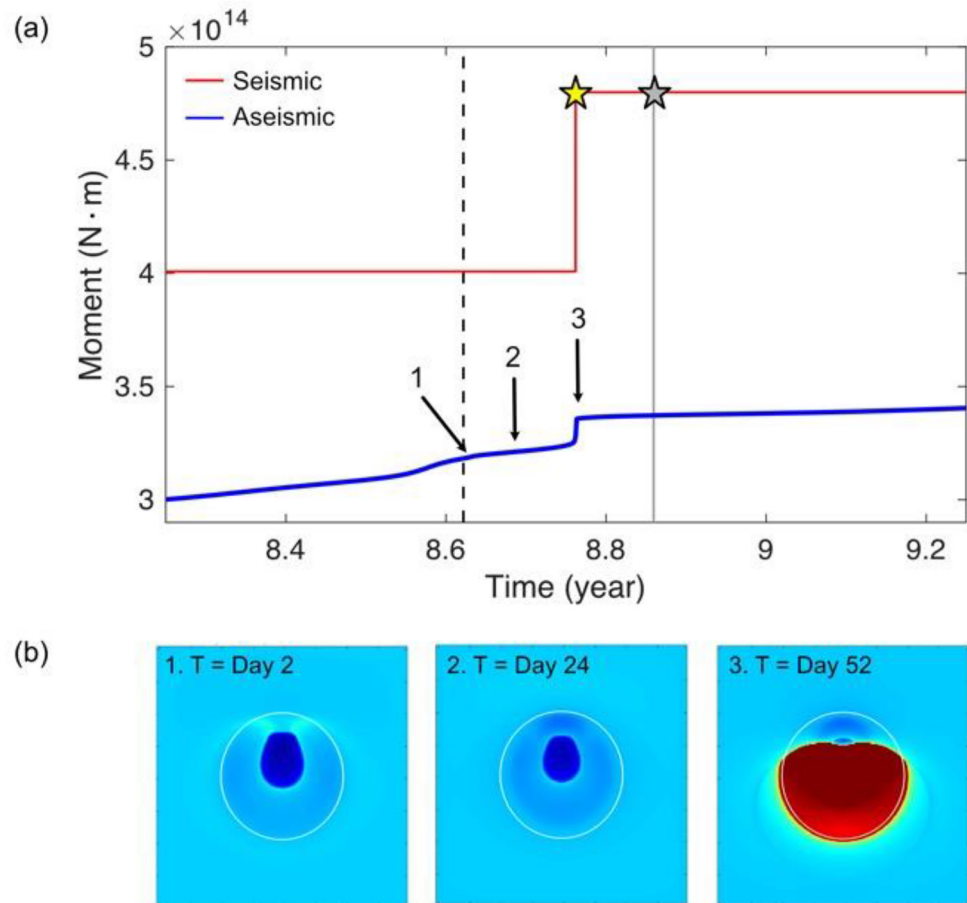
Figure 8. Simulation with $\Delta p = 0.1$ MPa and $T_p = 85\%$ (imposed in the fifth cycle) that results in an advancement of the triggered event. (a) The release of seismic and aseismic moment during the perturbed cycle. In this case, pore pressure is 0.1 MPa and = 85%. Yellow star represents the occurrence of the triggered event, which marks the beginning of the next cycle. The gray star and gray line represent the timing of the sixth event in the unperturbed sequence. In this case, the triggered event experiences a time advancement. (b) Snapshots illustrating the slip evolution on the VW patch after pore pressure is perturbed. Color scale used in this sub-figure is the same as that in Figure 7b.

the fault momentarily reaches 10^{-1} m/s and releases seismic moment equivalent to a M_w 0.9 earthquake (Figure S6).

4. Discussion

4.1. Implications for Induced Seismicity

Substantial aseismic moment release has been observed in both field- and lab-scale studies of induced earthquakes (McGarr & Barbour, 2018). Our numerical study finds that even small Δp of ≤ 0.2 MPa can induce substantial aseismic slip, which can change the temporal seismicity distribution, even if perturbation occurs toward the end of the interseismic period. In many studies, wells within 10 km from the induced earthquakes are typically included in the analyses. According to existing hydrogeological model calculations, the magnitude of pore pressure perturbation at distances between 2 and 10 km possibly falls within the lower end of our tested perturbation range, that is, less than 0.2 MPa. Also, since faults are believed to be critically stressed in intraplate regions as aforementioned (Townend & Zoback, 2000), that is, fault approaching the end of the seismic cycle, the modeled condition can be applicable for describing the continental interior prone to induced seismicity. Our results suggest that aseismic slip can play a crucial role in influencing the temporal evolution of earthquake sequences occurring in these regions. While it
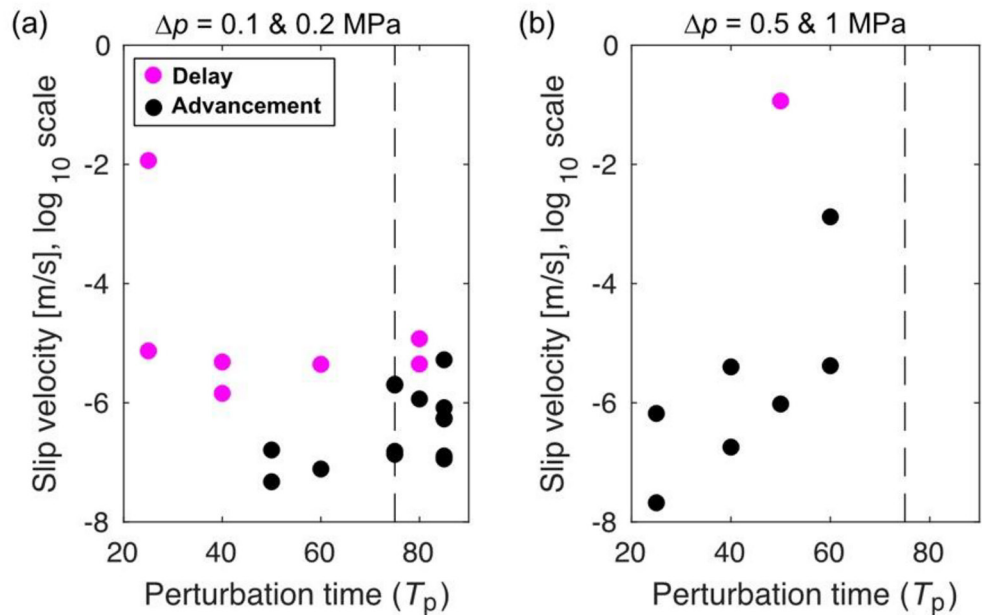
Figure 9. Maximum slip velocity of triggered aseismic transient due to pore pressure perturbation. (a) Cases with $\Delta p =$ 0.1 and 0.2 MPa. For $T_p \geq 75\%$, cases with perturbation occurring in the fourth and fifth earthquake cycles are also plotted. (b) Cases with $\Delta p =$ 0.5 and 1 MPa.

is challenging to determine the stress state of individual faults, our results imply that many earthquakes can possibly be delayed. For this reason, even though a decrease in seismicity is being observed in recent years after the reduction of injection operations (Langenbruch & Zoback, 2016), induced earthquakes as a phenomenon may last for longer than expected. In particular, a recent study on a seismic swarm in Western Canada shows that pore pressure-driven aseismic slip is likely the driving mechanism behind the unusually long-lived seismicity that persisted almost a year after the completion of hydraulic fracturing operations, which is also far longer than expected for a typical aftershock sequence for a mainshock of M_w 4.1 (Eyre et al., 2020). Broadband and borehole array catalog locations indicate that the seismic swarm appears to occur on multiple fault strands. While our current model simulates a single earthquake sequence on a planar fault, we argue that if the effects of triggered aseismic slip is prominent on an aggregate of critically stressed fault strands and modulate the earthquake cycles to various extents, the combined seismicity generated may appear as a prolonged series of events.

To this end, further investigation is required, as our model is simplified in terms of both the spatial and temporal distribution of pore pressure change. More complex perturbation patterns will be incorporated into the model based on realistic injection history. Future work will also focus on simulating more heterogeneous faults, such as one with multiple VW regions that can generate more sophisticated series of earthquake of different sizes. Nevertheless, our findings reinforce the importance of better instrumentation for close monitoring of fault motions, as the spatial and temporal evolution of aseismic slip could be valuable for predicting the likelihood of induced events occurring in the near future. For instance, one may be able to infer from dense arrays of borehole strainmeters measurable slow slip signal along the locked segment, characterizing their location and intensity. Borehole seismometers may improve the local magnitude of completeness and allow us to observe tiny seismic signals as discussed in Section 3.3, which may potentially be useful for predicting large earthquakes in the near future. Furthermore, since aseismic slip is dependent on the frictional properties of the fault, one may be able to obtain insightful information about the frictional properties in the region of interest based on observations of induced source properties and aseismic motions along fault.

4.2. Aseismic Slip Triggered by Other Types of Stress Perturbation

Pore pressure change is undeniably a major factor contributing to induced earthquakes, especially in regions where fluid pathways are available between injection source and nearby preexisting faults. On the other hand, both observational and numerical studies also suggested that the perturbation of solid matrix stress due to poroelastic response to injection or thermoelastic response from the temperature gradient between the injected fluids and the rocks also plays a role and may even take over fluid diffusion as the dominating triggering mechanism at large distances from injection wells (Deng et al., 2016; Goebel et al., 2017; Murphy et al., 2013; Segall & Lu, 2015). Therefore, it is also important to understand the potential of poroelastic stress change in triggering aseismic slip and its associated effects.

Extending from our model, we perform an analogous set of simulations with shear stress perturbed on the fault instead of pore pressure. Shear stress perturbation with similar magnitude range (between 0.1 and 1 MPa) is imposed as a positive step change at the same T_p mentioned in Section 2. Simulation results indicate that in the framework of rate-and-state frictions, poroelastic stress perturbation can also trigger significant aseismic response on the fault and cause similar extent of temporal modulations in earthquake cycles, including both advancement and delay of events (Figure S7). In certain cases, we also observe significant aseismic slip in subsequent earthquake cycle after a main event has been triggered (Figure S8). Our result implies that aseismic fault slip remains a key driver in the triggering process of seismicity under different types of stress perturbation.

5. Conclusions

In this study, we model the long-term fault response to pore pressure perturbation and study how perturbations can influence the aseismic behavior of a fault which can lead to modulation of earthquake cycles. We find that pore pressure perturbation can result in a wide range of aseismic responses, which can lead to both time advancement and delay of earthquake, as well as variations in the nucleation process, resulting in a wide range of nucleation size. The extent of aseismic slip is predominantly dependent on the magnitude of pore pressure change and state of the fault at the time of perturbation. In particular, our results highlight two key findings: (1) Even very small perturbation (<5% of the average event stress drop) is capable of inducing substantial aseismic response, which, depending on the time of perturbation, can lead to contrasting outcomes. (2) Triggered events that are delayed in time are associated with large aseismic moment release. In scenarios with small perturbations, it is possible to characterize critical conditions of aseismic transients that would determine the outcome of triggering. Also, as perturbation magnitude increases, there is also an increasing trend in the intensity of aseismic transients associated with delayed earthquakes. Our results have important implications for seismic hazard assessment, especially in the context of induced seismicity. With enhanced instrumentations and monitoring, one may be able to identify fault-specific critical patterns of aseismic motion that can cause earthquakes to occur sooner or later.

Data Availability Statement

Simulation data set supporting the analysis and conclusions is accessible through the University of Toronto Dataverse (https://doi.org/10.5683/SP2/BC9U5F).

References

Barbot, S., Lapusta, N., & Avouac, J.-P. (2012). Under the hood of the earthquake machine: Toward predictive modeling of the seismic cycle. *Science*, *336*(6082), 707–710. https://doi.org/10.1126/science.1218796

Ben-Zion, Y., & Rice, J. R. (1997). Dynamic simulations of slip on a smooth fault in an elastic solid. *Journal of Geophysical Research*, *102*(B8), 17771–17784. https://doi.org/10.1029/97jb01341

Bhattacharya, P., & Viesca, R. C. (2019). Fluid-induced aseismic fault slip outpaces pore-fluid migration. *Science*, *364*(6439), 464–468. https://doi.org/10.1126/science.aaw7354

Bizzarri, A., & Belardinelli, M. E. (2008). Modeling instantaneous dynamic triggering in a 3-D fault system: Application to the 2000 June South Iceland seismic sequence. *Geophysical Journal International*, *173*(3), 906–921. https://doi.org/10.1111/j.1365-246x.2008.03765.x

Boyd, O. S., McNamara, D. E., Hartzell, S., & Choy, G. (2017). Influence of lithostatic stress on earthquake stress drops in North America. *Bulletin of the Seismological Society of America*, *107*(2), 856–868. https://doi.org/10.1785/0120160219

Byrne, D. E., Sykes, L. R., & Davis, D. M. (1992). Great thrust earthquakes and aseismic slip along the plate boundary of the Makran Subduction Zone. *Journal of Geophysical Research*, *97*(B1), 449–478. https://doi.org/10.1029/91jb02165

Cappa, F., Scuderi, M. M., Collettini, C., Guglielmi, Y., & Avouac, J.-P. (2019). Stabilization of fault slip by fluid injection in the laboratory and in situ. *Science Advances*, *5*(3), eaau4065. https://doi.org/10.1126/sciadv.aau4065

Chen, T., & Lapusta, N. (2009). Scaling of small repeating earthquakes explained by interaction of seismic and aseismic slip in a rate and state fault model: Simulations of repeating earthquakes. *Journal of Geophysical Research*, *114*(B1). https://doi.org/10.1029/2008jb005749

Cornet, F. H. (2000). Comment on 'Large-scale in situ permeability tensor of rocks from induced microseismicity' by S. A. Shapiro, P. Audigane, and J.-J. Royer. *Geophysical Journal International*, *140*(2), 465–469. https://doi.org/10.1046/j.1365-246x.2000.00018.x

Day, S. M., Dalguer, L. A., Lapusta, N., & Liu, Y. (2005). Comparison of finite difference and boundary integral solutions to three-dimensional spontaneous rupture. *Journal of Geophysical Research*, *110*(B12), B12307. https://doi.org/10.1029/2005jb003813

De Barros, L., Cappa, F., Deschamps, A., & Dublanchet, P. (2020). Imbricated aseismic slip and fluid diffusion drive a seismic swarm in the Corinth Gulf, Greece. *Geophysical Research Letters*, *47*(9), e2020GL087142. https://doi.org/10.1029/2020gl087142

De Barros, L., Daniel, G., Guglielmi, Y., Rivet, D., Caron, H., Payre, X., et al. (2016). Fault structure, stress, or pressure control of the seismicity in shale? Insights from a controlled experiment of fluid-induced fault reactivation. *Journal of Geophysical Research: Solid Earth*, *121*(6), 4506–4522. https://doi.org/10.1002/2015jb012633

Deng, K., Liu, Y., & Harrington, R. M. (2016). Poroelastic stress triggering of the December 2013 Crooked Lake, Alberta, induced seismicity sequence. *Geophysical Research Letters*, *43*(16), 8482–8491. https://doi.org/10.1002/2016gl070421

Dieterich, J. (1994). A constitutive law for rate of earthquake production and its application to earthquake clustering. *Journal of Geophysical Research*, *99*(B2), 2601–2618. https://doi.org/10.1029/93jb02581

Dieterich, J. H. (1979). Modeling of rock friction: 1. Experimental results and constitutive equations. *Journal of Geophysical Research*, *84*(B5), 2161–2168. https://doi.org/10.1029/jb084ib05p02161

Duboeuf, L., De Barros, L., Cappa, F., Guglielmi, Y., Deschamps, A., & Seguy, S. (2017). Aseismic motions drive a sparse seismicity during fluid injections into a fractured zone in a carbonate reservoir. *Journal of Geophysical Research: Solid Earth*, *122*(10), 8285–8304. https://doi.org/10.1002/2017jb014535

Duverger, C., Lambotte, S., Bernard, P., Lyon-Caen, H., Deschamps, A., & Nercessian, A. (2018). Dynamics of microseismicity and its relationship with the active structures in the western Corinth Rift (Greece). *Geophysical Journal International*, *215*(1), 196–221. https://doi.org/10.1093/gji/ggy264

Eyre, T. S., Eaton, D. W., Garagash, D. I., Zecevic, M., Venieri, M., Weir, R., & Lawton, D. C. (2019). The role of aseismic slip in hydraulic fracturing–induced seismicity. *Science Advances*, *5*(8), eaav7172. https://doi.org/10.1126/sciadv.aav7172

Eyre, T. S., Zecevic, M., Salvage, R. O., & Eaton, D. W. (2020). A long-lived swarm of hydraulic fracturing-induced seismicity provides evidence for aseismic slip. *Bulletin of the Seismological Society of America*, *110*(5), 2205–2215. https://doi.org/10.1190/segam2020-3421625

Goebel, T. H. W., Weingarten, M., Chen, X., Haffener, J., & Brodsky, E. E. (2017). The 2016 Mw5.1 Fairview, Oklahoma earthquakes: Evidence for long-range poroelastic triggering at >40 km from fluid disposal wells. *Earth and Planetary Science Letters*, *472*, 50–61. https://doi.org/10.1016/j.epsl.2017.05.011

Gomberg, J., Beeler, N. M., Blanpied, M. L., & Bodin, P. (1998). Earthquake triggering by transient and static deformations. *Journal of Geophysical Research*, *103*(B10), 24411–24426. https://doi.org/10.1029/98jb01125

Goodfellow, S. D., Nasseri, M. H. B., Maxwell, S. C., & Young, R. P. (2015). Hydraulic fracture energy budget: Insights from the laboratory. *Geophysical Research Letters*, *42*(9), 3179–3187. https://doi.org/10.1002/2015gl063093

Guglielmi, Y., Cappa, F., Avouac, J.-P., Henry, P., & Elsworth, D. (2015). Seismicity triggered by fluid injection-induced aseismic slip. *Science*, *348*(6240), 1224–1226. https://doi.org/10.1126/science.aab0476

Hatch, R. L., Abercrombie, R. E., Ruhl, C. J., & Smith, K. D. (2020). Evidence of aseismic and fluid-driven processes in a small complex seismic swarm near Virginia City, Nevada. *Geophysical Research Letters*, *47*(4), e2019GL085477. https://doi.org/10.1029/2019gl085477

Hearn, E. H., Koltermann, C., & Rubinstein, J. L. (2018). Numerical models of pore pressure and stress changes along basement faults due to wastewater injection: Applications to the 2014 Milan, Kansas Earthquake. *Geochemistry, Geophysics, Geosystems*, *19*(4), 1178–1198. https://doi.org/10.1002/2017gc007194

Huang, Y., De Barros, L., & Cappa, F. (2019). Illuminating the rupturing of microseismic sources in an injection-induced earthquake experiment. *Geophysical Research Letters*, *46*(16), 9563–9572. https://doi.org/10.1029/2019gl083856

Huang, Y., Ellsworth, W. L., & Beroza, G. C. (2017). Stress drops of induced and tectonic earthquakes in the central United States are indistinguishable. *Science Advances*, *3*(8), e1700772. https://doi.org/10.1126/sciadv.1700772

Igarashi, T., Matsuzawa, T., & Hasegawa, A. (2003). Repeating earthquakes and interplate aseismic slip in the northeastern Japan subduction zone. *Journal of Geophysical Research*, *108*(B5), 2249. https://doi.org/10.1029/2002jb001920

Jolivet, R., Simons, M., Agram, P. S., Duputel, Z., & Shen, Z.-K. (2015). Aseismic slip and seismogenic coupling along the central San Andreas Fault. *Geophysical Research Letters*, *42*(2), 297–306. https://doi.org/10.1002/2014gl062222

Keranen, K. M., & Weingarten, M. (2018). Induced seismicity. *Annual Reviews of Earth and Planetary Sciences*, *28*, 149–174. https://doi.org/10.1146/annurev-earth-082517-010054

Keranen, K. M., Weingarten, M., Abers, G. A., Bekins, B. A., & Ge, S. (2014). Sharp increase in central Oklahoma seismicity since 2008 induced by massive wastewater injection. *Science*, *345*(6195), 448–451. https://doi.org/10.1126/science.1255802

Langenbruch, C., & Zoback, M. D. (2016). How will induced seismicity in Oklahoma respond to decreased saltwater injection rates? *Science Advances*, *2*(11), e1601542. https://doi.org/10.1126/sciadv.1601542

Lapusta, N., & Liu, Y. (2009). Three-dimensional boundary integral modeling of spontaneous earthquake sequences and aseismic slip. *Journal of Geophysical Research*, *114*(B9), B09303. https://doi.org/10.1029/2008jb005934

Lapusta, N., & Rice, J. R. (2003). Nucleation and early seismic propagation of small and large events in a crustal earthquake model: Nucleation and early seismic propagation. *Journal of Geophysical Research*, *108*(B4), 2205. https://doi.org/10.1029/2001jb000793

Lapusta, N., Rice, J. R., Ben-Zion, Y., & Zheng, G. (2000). Elastodynamic analysis for slow tectonic loading with spontaneous rupture episodes on faults with rate- and state-dependent friction. *Journal of Geophysical Research*, *105*(B10), 23765–23789. https://doi.org/10.1029/2000jb900250

Loken, C., Gruner, D., Groer, L., Peltier, R., Bunn, N., Craig, M., et al. (2010). SciNet: Lessons learned from building a power-efficient top-20 system and data center. *Journal of Physics*, *256*, 012026. https://doi.org/10.1088/1742-6596/256/1/012026

Lui, S. K. Y., & Lapusta, N. (2016). Repeating microearthquake sequences interact predominantly through postseismic slip. *Nature Communications*, *7*(1), 13020. https://doi.org/10.1038/ncomms13020

Lui, S. K. Y., & Lapusta, N. (2018). Modeling high stress drops, scaling, interaction, and irregularity of repeating earthquake sequences near parkfield. *Journal of Geophysical Research*, *123*(12), 10854–10879. https://doi.org/10.1029/2018jb016472

Marone, C. (1998). Laboratory-derived friction laws and their application to seismic faulting. *Annual Review of Earth and Planetary Sciences*, *26*(1), 643–696. https://doi.org/10.1146/annurev.earth.26.1.643

McGarr, A., & Barbour, A. J. (2018). Injection-induced moment release can also be aseismic. *Geophysical Research Letters*, *45*(11), 5344–5351. https://doi.org/10.1029/2018gl078422

Miyazaki, S., Segall, P., McGuire, J. J., Kato, T., & Hatanaka, Y. (2006). Spatial and temporal evolution of stress and slip rate during the 2000 Tokai slow earthquake: THE 2000 Tokai slow earthquake. *Journal of Geophysical Research*, *111*(B3). https://doi.org/10.1029/2004jb003426

Murphy, S., O'Brien, G. S., McCloskey, J., Bean, C. J., & Nalbant, S. (2013). Modeling fluid induced seismicity on a nearby active fault. *Geophysical Journal International*, *194*(3), 1613–1624. https://doi.org/10.1093/gji/ggt174

Nadeau, R. M., & Johnson, L. R. (1998). SVI: Moment release rates and estimates of source parameters for small repeating earthquakes. *Bulletin of the Seismological Society of America*, *88*(3), 790–814

Noda, H., & Lapusta, N. (2013). Stable creeping fault segments can become destructive as a result of dynamic weakening. *Nature*, *493*(7433), 518–521. https://doi.org/10.1038/nature11703

Noda, H., Lapusta, N., & Kanamori, H. (2013). Comparison of average stress drop measures for ruptures with heterogeneous stress change and implications for earthquake physics. *Geophysical Journal International*, *193*(3), 1691–1712. https://doi.org/10.1093/gji/ggt074

Parotidis, M., Rothert, E., & Shapiro, S. A. (2003). Pore-pressure diffusion: A possible triggering mechanism for the earthquake swarms 2000 in Vogtland/NW-Bohemia, central Europe: A swarm earthquake triggering mechanism. *Geophysical Research Letters*, *30*(20). https://doi.org/10.1029/2003gl018110

Ponce, M., van Zon, R., Northrup, S., Gruner, D., Chen, J., Ertinaz, F., et al. (2019). Deploying a top-100 supercomputer for large parallel workloads: The Niagara supercomputer. In *Proceedings of the practice and experience in advanced Research computing on rise of the machines (learning)* (pp. 1–8). New York, NY, USA: Association for Computing Machinery. Retrieved from https://doi.org/10.1145/3332186.3332195

Rice, J. R., Lapusta, N., & Ranjith, K. (2001). Rate and state dependent friction and the stability of sliding between elastically deformable solids. *Journal of the Mechanics and Physics of Solids*, *49*(9), 1865–1898. https://doi.org/10.1016/s0022-5096(01)00042-4

Rice, J. R., & Ruina, A. L. (1983). Stability of steady frictional slipping. *Journal of Applied Mechanics*, *50*(2), 343–349. https://doi.org/10.1115/1.3167042

Rousset, B., Jolivet, R., Simons, M., Lasserre, C., Riel, B., Milillo, P., et al. (2016). An aseismic slip transient on the North Anatolian Fault. *Geophysical Research Letters*, *43*(7), 3254–3262. https://doi.org/10.1002/2016gl068250

Rubin, A. M., & Ampuero, J.-P. (2005). Earthquake nucleation on (aging) rate and state faults: Rate and state earthquake nucleation. *Journal of Geophysical Research*, *110*(B11). https://doi.org/10.1029/2005jb003686

Ruhl, C. J., Abercrombie, R. E., Smith, K. D., & Zaliapin, I. (2016). Complex spatiotemporal evolution of the 2008 M w 4.9 Mogul earthquake swarm (Reno, Nevada): Interplay of fluid and faulting. *Journal of Geophysical Research: Solid Earth*, *121*(11), 8196–8216. https://doi.org/10.1002/2016jb013399

Ruina, A. (1983). Slip instability and state variable friction laws. *Journal of Geophysical Research*, *88*(B12), 10359–10370. https://doi.org/10.1029/jb088ib12p10359

Schaal, N., & Lapusta, N. (2019). Microseismicity on patches of higher compression during larger-scale earthquake nucleation in a rate-and-state fault model. *Journal of Geophysical Research: Solid Earth*, *124*(2), 1962–1990. https://doi.org/10.1029/2018jb016395

Schmidt, D. A., Bürgmann, R., Nadeau, R. M., & d'Alessio, M. (2005). Distribution of aseismic slip rate on the Hayward fault inferred from seismic and geodetic data. *Journal of Geophysical Research*, *110*(B8). https://doi.org/10.1029/2004jb003397

Segall, P. (1989). Earthquakes triggered by fluid extraction. *Geologica*, *17*(10), 942–946. https://doi.org/10.1130/0091-7613(1989)017<0942:etbfe>2.3.co;2

Segall, P., & Lu, S. (2015). Injection-induced seismicity: Poroelastic and earthquake nucleation effects. *Journal of Geophysical Research: Solid Earth*, *120*(7), 5082–5103. https://doi.org/10.1002/2015jb012060

Shapiro, S. A., Rothert, E., Rath, V., & Rindschwentner, J. (2002). Characterization of fluid transport properties of reservoirs using induced microseismicity. *Geophysics*, *67*(1), 212–220. https://doi.org/10.1190/1.1451597

Townend, J., & Zoback, M. D. (2000). How faulting keeps the crust strong. *Geology*, *28*(5), 399–402. https://doi.org/10.1130/0091-7613(2000)028<0399:hfktcs>2.3.co;2

Wei, S., Avouac, J.-P., Hudnut, K. W., Donnellan, A., Parker, J. W., Graves, R. W., et al. (2015). The 2012 Brawley swarm triggered by injection-induced aseismic slip. *Earth and Planetary Science Letters*, *422*, 115–125. https://doi.org/10.1016/j.epsl.2015.03.054

Wu, Q., Chapman, M., & Chen, X. (2018). Stress-drop variations of induced earthquakes in Oklahoma. *Bulletin of the Seismological Society of America*, *108*(3A), 1107–1123. https://doi.org/10.1785/0120170335